State-selective probing of CO_2 autoionizing inner valence Rydberg states with attosecond extreme ultraviolet four-wave-mixing spectroscopy

Ashley P. Fidler,[1,2,*,†] Yen-Cheng Lin,[1,2,*] James D. Gaynor,[1,2] C. William McCurdy,[1,3] Stephen R. Leone,[1,2,4] Robert R. Lucchese,[1] and Daniel M. Neumark[1,2]

[1]*Chemical Sciences Division, Lawrence Berkeley National Laboratory, Berkeley, California 94720, USA*
[2]*Department of Chemistry, University of California, Berkeley, Berkeley, California 94720, USA*
[3]*Department of Chemistry, University of California, Davis, Davis, California 95616, USA*
[4]*Department of Physics, University of California, Berkeley, Berkeley, California, 94720, USA*

(Received 15 October 2022; accepted 7 December 2022; published 30 December 2022)

Nonlinear spectroscopies can disentangle spectra that are congested due to inhomogeneous broadening. In conjunction with theoretical calculations, attosecond extreme ultraviolet (XUV) four-wave-mixing (FWM) spectroscopy is utilized here to probe the dynamics of autoionizing inner valence excited Rydberg states of the polyatomic molecule, CO_2. This tabletop nonlinear technique employs a short attosecond XUV pulse train and two noncollinear, few-cycle near-infrared pulses to generate background-free XUV wave-mixing signals. FWM emission is observed from the $n = 5$–7 states of the Henning sharp $nd\sigma_g$ Rydberg series that converges to the ionic $\tilde{B}\ ^2\Sigma_u^+$ state. However, these transient emission signals decay with lifetimes of 33 ± 6, 53 ± 2, and 94 ± 2 fs, respectively, which calculations show are consistent with the lifetimes of the short-lived $n = 6$–8 members of the $ns\sigma_g$ character Henning diffuse Rydberg series. The oscillator strengths of transitions between states involved in all possible resonant FWM processes are calculated, verifying that the nonlinear spectra are dominated by pathways described by an initial excitation to the diffuse $ns\sigma_g$ Rydberg series and emission from the sharp $nd\sigma_g$ Rydberg series. The results substantiate not only that attosecond XUV FWM spectroscopy produces rigorous and meaningful measurements of ultrafast dynamics in polyatomic systems, but also that nonlinear spectroscopic techniques are versatile tools to selectively probe dynamics that are otherwise difficult to access.

DOI: 10.1103/PhysRevA.106.063525

I. INTRODUCTION

Nonlinear spectroscopies are exceptionally powerful tools that can elucidate complex structure and dynamics in chemical systems. In these techniques, multiple short coherent light pulses interact with matter to generate a higher-order polarization response [1,2]. While linear spectroscopy has been effectively employed to provide energetic and structural information, the remarkable versatility of nonlinear methods originates from experimental control over the frequency, intensity, beam geometry, and sequence of each of the incoming pulses. These additional degrees of freedom allow for highly selective measurements in both the frequency and time domains, permitting diverse applications such as probing structure and dynamics in complex chemical systems [3–5], disentangling homogeneous and inhomogeneous line widths, [6] and modifying the spectral bandwidth of light sources [7,8]. The extension of nonlinear spectroscopies into the extreme ultraviolet (XUV) and x-ray spectral regions will enable experiments that investigate short-lived and element-specific inner valence and core-excited states with greater spatial and temporal resolution [9–12], further expanding the frontiers of these important techniques.

The development of high harmonic generation (HHG) [13,14] over the past three decades has resulted in accessible tabletop coherent XUV sources with subfemtosecond pulse durations [15]. The extremely short time resolution of these attosecond light sources not only permits direct time-domain measurements of electronic dynamics in atomic [16–18], molecular [19–21], and solid-state systems [22–24], but also provides the foundation for tabletop versions of XUV nonlinear spectroscopy. A recently developed extension of these techniques [25,26], attosecond XUV four-wave-mixing (FWM) spectroscopy, utilizes a short attosecond XUV pulse train produced by HHG and two noncollinear near-infrared (NIR) pulses to generate spatially isolated third-order polarization signals. These transient emission signals encode the evolution of excited states and represent background-free measurements of XUV-induced chemical dynamics [27–29]. This technique has already been applied to monitor electronic and vibronic coherences in multiple atomic and diatomic systems [21,25,26], facilitating the characterization of a previously inaccessible dark state in N_2 [30], the detection of light-induced states in He [31], and the implementation of a variant of XUV multidimensional spectroscopy in long-lived Rydberg states of Ar [32]. Moreover, attosecond wave-mixing experiments have revealed order-dependent emission delays in nonlinear signal generation [33] and measured ultrafast dy-

*These authors contributed equally to this work.
†Present address: Department of Chemistry, Princeton University, Princeton, NJ 08544, USA.

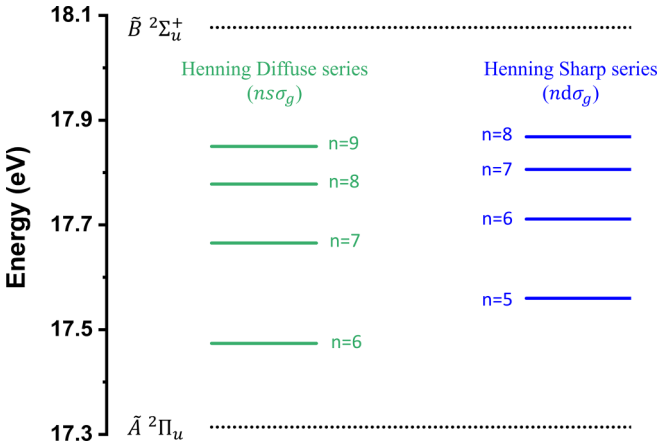

FIG. 1. Energy level diagram of the Henning diffuse (green) and Henning sharp (blue) Rydberg series of CO_2 between 17.3 and 18.1 eV. Dotted lines represent ionic states while solid lines represent neutral Rydberg states. Both the $ns\sigma_g$ character Henning diffuse and $nd\sigma_g$ character Henning sharp series converge to the ionic $\tilde{B}\ ^2\Sigma_u^+$ state.

namics due to autoionization and Auger decay in atomic [27], diatomic [28], and solid-state systems [29]. Here, we extend attosecond XUV FWM spectroscopy to probe autoionization dynamics in a polyatomic system, the inner valence Rydberg states of carbon dioxide.

As a linear triatomic, centrosymmetric molecule composed of only second row elements, CO_2 is one of the simplest polyatomic systems. CO_2 attracts considerable interest from molecular spectroscopists and the broader scientific community as a well-known greenhouse gas with notable impacts on climate [34]. Of particular relevance to the current work, the electronic structure of CO_2 and its low-lying ionic states has been characterized by photoabsorption, photoionization, and photoelectron spectroscopy [35–43]. The lowest four ionic states of CO_2 are the $\tilde{X}\ ^2\Pi_g$, $\tilde{A}\ ^2\Pi_u$, $\tilde{B}\ ^2\Sigma_u^+$, and $\tilde{C}\ ^2\Sigma_g^+$ states reached by ionization energies of 13.778, 17.314, 18.077, and 19.394 eV, respectively. In our experiment, an XUV pulse predominantly excites CO_2 into neutral Rydberg states located between 17.3 and 18.1 eV. An energy level diagram depicting the XUV-excited states relevant to this experiment is provided in Fig. 1. This spectral region of CO_2 contains contributions from the Henning diffuse and Henning sharp series, both of which converge to the ionic $\tilde{B}\ ^2\Sigma_u^+$ threshold, as well as the Tanaka-Ogawa series, which converges to the ionic $\tilde{A}\ ^2\Pi_u$ threshold [39,40,42]. The two Henning series dominate the photoabsorption spectrum, as contributions from the Tanaka-Ogawa series are limited to members with both high n and ν_1 quantum numbers in the spectral region above the $\tilde{A}\ ^2\Pi_u$ limit examined here. Complementary experiments by Sandhu and co-workers probing the dynamics of the Tanaka-Ogawa series are currently underway [44].

The Henning diffuse and Henning sharp series are assigned Rydberg electron characters of $ns\sigma_g$ and $nd\sigma_g$, respectively. While weak transitions to the $\nu_1 = 1$ symmetric stretch have been observed in the photoabsorption spectra, the $\nu_1 = 0$ transition dominates [35]. Photoionization quantum efficiency measurements provide insight into the channels relevant in the decay dynamics of these series [40]. For the Henning diffuse series, the photoionization quantum efficiency is close to unity, indicating that autoionization is the dominant decay pathway for this series. On the other hand, in the same work, the photoionization quantum efficiency of the Henning sharp series is notably less than unity, possibly reflecting competition between neutral predissociation and autoionization. While these photoionization measurements and the spectral linewidths of the states suggest that members of the Henning diffuse series decay more quickly than those of the Henning sharp series, more work is necessary to establish the lifetimes of these states.

In this joint experimental-theoretical work, we utilize attosecond FWM spectroscopy to investigate the ultrafast decay dynamics of autoionizing Rydberg states of CO_2. Spatially isolated FWM emission signals are primarily observed at energies associated with members of the Henning sharp series between 17.3 and 18.1 eV. However, time-resolved measurements, supported by theoretical calculations of autoionization lifetimes, reveal that these emission signals report on the dynamics of members of the shorter-lived Henning diffuse series instead. Specifically, the experimentally measured decays of 33 ± 6, 53 ± 2, and 94 ± 2 fs correspond well to the lifetimes of the $n = 6$–8 Henning diffuse states calculated here. The interpretation of this counterintuitive result is facilitated by calculating oscillator strengths for transitions between states that may participate in the various resonant wave-mixing schemes. These calculations indicate that, due to substantial ground-to-diffuse state and dark-to-sharp state oscillator strengths, wave-mixing pathways dominate that probe the Henning diffuse states but emit from members of the Henning sharp series, as observed experimentally. This attosecond XUV FWM experiment demonstrates that transient wave mixing can be successfully utilized to monitor ultrafast decay in polyatomic molecules with high selectivity.

II. METHODS

A. Experimental methods

The experimental apparatus utilized to generate and measure XUV emission signals has been described previously [27–30,33] and is depicted in Fig. 2(a). Briefly, a commercial multipass Ti:sapphire laser system (Femtopower HE, Femtolasers) produces 2 mJ of 22 fs NIR pulses with a central wavelength of 780 nm at a 1 kHz repetition rate. These pulses are spectrally broadened in a stretched 2 m long, 500 μm inner diameter hollow core fiber (Few-Cycle Inc.) statically filled with 2 bars of neon gas. The broadband fiber output is then temporally recompressed by seven pairs of double-angle chirped mirrors (PC70, Ultrafast Innovations) and a 2 mm thick ammonium dihydrogen phosphate (ADP) crystal [45], resulting in 600 μJ, 6 fs pulses with a spectral profile spanning 550 to 950 nm [Fig. 2(b)]. A 75:25 (T:R) beam splitter divides the compressed NIR pulses into two arms. The transmitted portion of the beam is focused by a spherical silver mirror ($f = 50$ cm) through 300 μm holes drilled into a 1 mm path-length cell contained within a vacuum chamber at 10^{-6} Torr. The interaction of the focused NIR driver ($\sim 10^{14}$ W cm^{-2}) with xenon gas flowing through the cell produces XUV harmonics via high harmonic generation

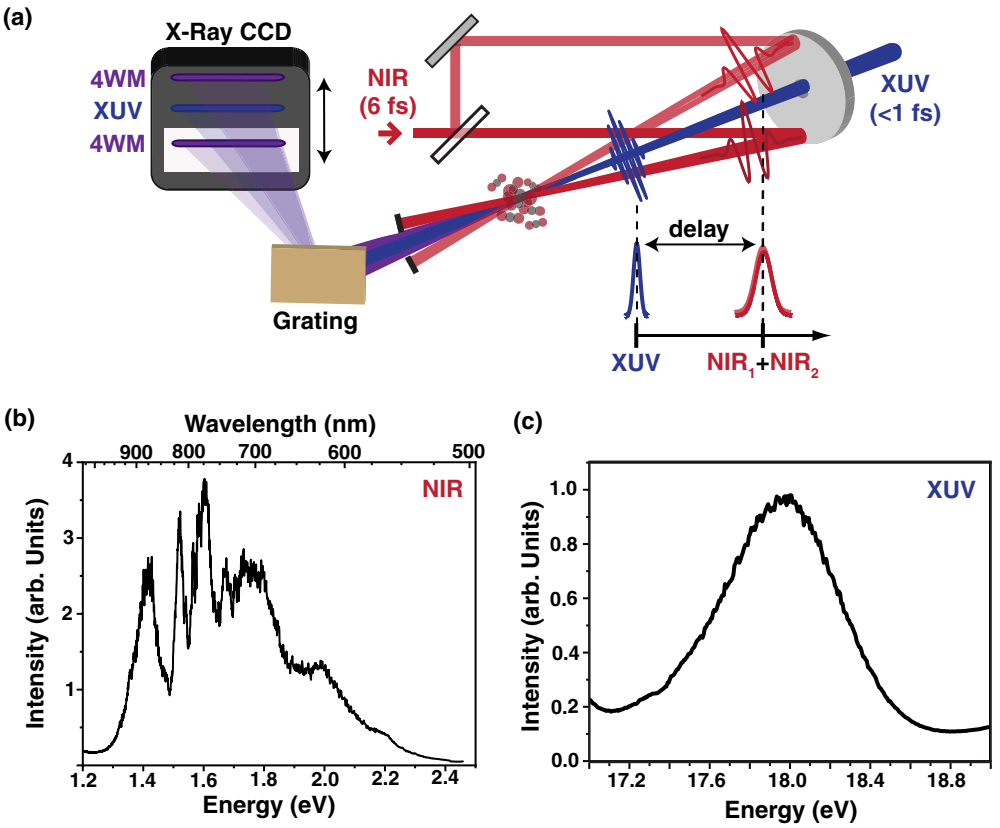

FIG. 2. Attosecond extreme ultraviolet (XUV) four-wave-mixing (FWM) spectroscopy. (a) Subfemtosecond XUV pulses at ∼18 eV produced via high harmonic generation and two few-femtosecond (780 nm) NIR pulses are utilized to generate XUV wave-mixing emission signals from Rydberg states in gas-phase carbon dioxide. (b) Spectrum of NIR pulse. (c) Spectrum of XUV pulse.

(HHG). The pressure of xenon gas (∼5 Torr) flowing through the cell and its position relative to the few-cycle NIR driver pulse focus are optimized to generate a train of two to three subfemtosecond XUV pulses with photon energies that cover the neutral Rydberg states of CO_2 located between 17.3 and 18.1 eV [Fig. 2(c)]. A 0.15 μm thick Al foil (Lebow) filters out the copropagating NIR driver before the transmitted XUV pulse train is focused by a gold-coated toroidal mirror ($f = 50$ cm, ARW Optical Corporation) through an annular mirror into a 1 mm path-length target cell. Small 500 μm diameter holes drilled into the target cell permit the XUV light to interact with the CO_2 gas flowing continuously though the cell. At the target cell, the XUV beam has an estimated waist of ∼20 μm and a peak intensity of the order of 10^8–10^{10} W cm^{-2} due to the low conversion efficiency of HHG [46].

The few-cycle NIR pulses reflected by the 75:25 beam splitter are delayed relative to the XUV pulse train by a piezoelectric stage [P-622 with E509 controller, Physik Instrumente (PI)] and then split into two distinct NIR arms by a 50:50 beam splitter. Two spherical mirrors ($f = 1$ m) direct each of the split beams into the vacuum chamber to positions above and below a 3 mm hole in the annular mirror through which the XUV pulse train passes. The focused upper and lower NIR beams intersect with the XUV in the target cell at angles of approximately 18 mrad (1.0°). To ensure that the NIR pulses arrive at the target simultaneously, the path length of the lower NIR arm is adjusted with a second piezoelectric stage. Temporal and spatial overlap between the XUV and NIR arms is determined via second harmonic generation in a BBO crystal. Specifically, the removal of the Al foil that blocks the copropagating NIR after HHG allows a mirror inserted after the annular mirror to steer all three NIR beams out of the vacuum chamber to a BBO crystal located at the focus of the NIR driver. At overlap, second harmonic signals emit at phase-matching angles intermediate between each of the noncollinear NIR beams.

After passing through the target cell, the XUV harmonics and any generated nonlinear XUV emission signals transit through a slit that blocks the angled NIR beams. Residual NIR contamination is further attenuated by a second 0.15 μm Al filter before the transmitted XUV light is spectrally dispersed by a gold-coated flat-field grating (001-0639, Hitachi). An x-ray charge-coupled device (CCD) camera (Pixis XO 400B, Princeton Instruments) records the target-attenuated harmonics and wave-mixing emission signals on a 1340 × 400 pixel array as a function of XUV photon energy and phase-matched divergence angle relative to the harmonic axis. The horizontal energy axis is calibrated by comparing wave-mixing emission from the $2s^2 2p^5 nl$ excitations of neon gas to atomic line transition data available from the National Institute of Standards and Technology (NIST). In these experiments, a home-built mount translates the camera vertically such that the harmonics no longer impinge on the CCD chip and only wave-mixing

signals that emit at nonzero divergence angles are recorded. This spatial masking procedure is performed to reduce interference from artifacts induced by strong absorption features, allowing the weaker wave-mixing emission signals to be imaged cleanly.

CCD camera images are collected as a function of XUV-NIR delay, where positive delays are defined to indicate that the XUV pulse train precedes the time-coincident NIR pulses. Three datasets are collected under different experimental conditions to establish the reproducibility of measured decay times. These conditions are summarized in Appendix A. To enhance the relatively weak wave-mixing emission signals, all emission data are plotted in absorbance (A) (negative features):

$$A = -\log_{10}(I_{\text{NIR ON}}/I_{\text{NIR OFF}}), \tag{1}$$

where $I_{\text{NIR ON}}$ and $I_{\text{NIR OFF}}$ represent the signal collected by the CCD camera with all three beams impinging on the target and with both NIR pulses blocked by a mechanical shutter (Thorlabs), respectively. All subsequent data analysis was performed in MATLAB.

B. Theoretical methods

To explore the autoionization lifetimes of the Henning diffuse and Henning sharp Rydberg series in CO_2, we performed photoionization calculations very similar to those reported in Ref. [28] at the equilibrium geometry of the CO_2 molecule. We employed the multichannel Schwinger configuration interaction (MCSCI) variational method [47,48], which has been previously used to study the photoionization of CO_2 [49,50]. In these calculations, the final-state fixed-energy photoelectron wave functions were represented on a single-center expanded grid, with $l_{\max} = 100$, that terminated at $r_{\max} = 60$ Å, which was large enough to describe a number of Rydberg states below each ionization threshold. The full N-electron ionized state was represented as a close-coupling expansion containing a sum of the products of $(N-1)$-electron ion state wave functions with one-electron photoelectron continuum wave functions. The ion channels used in the close-coupling calculation included the four valence ion states, $(1\pi_g)^{-1}\ \tilde{X}\ ^2\Pi_g$, $(1\pi_u)^{-1}\ \tilde{A}\ ^2\Pi_u$, $(3\sigma_u)^{-1}\ \tilde{B}\ ^2\Sigma_u^+$, and $(4\sigma_g)^{-1}\ \tilde{C}\ ^2\Sigma_g^+$. The calculations were performed with the bond length $R_{\text{C–O}} = 1.1621$ Å [51]. The bound state orbitals were computed using an aug-cc-pVTZ basis [52,53] using MOLPRO [54,55] with a valence complete-active-space self-consistent field (VCASSCF) description of the ground state keeping the C($1s$) and O($1s$) core orbitals doubly occupied in all configuration state functions. In the photoionization calculation, the initial state was represented by a configuration interaction wave function with the three core orbitals doubly occupied and including up to quadrupole excitation into the weakly occupied orbitals from the VCASSCF calculation. The initial $^1\Sigma_g^+$ state used to compute the dipole matrix elements was then obtained using triple excitations into the weakly occupied orbitals. In the scattering calculations, the ionization potentials for the four ion states were adjusted to agree with experimental values of 13.78, 17.31, 18.08, and 19.39 eV for the $\tilde{X}$, $\tilde{A}$, $\tilde{B}$, and $\tilde{C}$ states, respectively [38]. The resulting cross sections contained a number of autoionizing resonance structures, which were analyzed by fitting the line shapes to Fano profiles [56] to extract the position and the width of each autoionization resonance.

Additionally, we located the position of an optically dark autoionizing state of symmetry $^1\Sigma_g^+$ that cannot be reached by a one-photon transition from the ground state and has a computed energy that is 15.8 eV above the ground state. To assess the extent to which this state could contribute to the FWM process, we then computed the oscillator strengths for transitions from this state to the bright Rydberg autoionizing states and the oscillator strengths from the ground state to the same bright states. These oscillator strengths were obtained using a purely bound state calculation, which was performed with the same MCSCI code that was used in the scattering calculations. In these calculations, we extended the aug-cc-pVTZ basis set used in the main scattering calculations with a set of Rydberg-like Gaussian basis functions of Kaufmann *et al.* [57] as defined by Eq. (18) of that paper. The added Gaussian functions had $l = 0$ with $n = 1.5,\ 2.0,\ \ldots,\ 6.0$, $l = 1$ with $n = 2.0,\ 2.5,\ \ldots,\ 4.0$, and $l = 2$ with $n = 2.5, 3.0, \ldots, 7.0$, where these 25 added functions all had σ symmetry.

III. RESULTS

A. Spatially isolated wave-mixing emission in carbon dioxide

The XUV pulse train generates a coherence of autoionizing Rydberg states of carbon dioxide spanning 17.3–18.1 eV, including members of the Henning diffuse and Henning sharp series [40,42]. This coherence is probed by two time-coincident, noncollinear NIR pulses, resulting in transient wave-mixing signals that emit at a spatial location distinct from the XUV harmonics dictated by wave-vector phase-matching conditions [Fig. 3(a)]. For a FWM process requiring both NIR beams, the wave-mixing signals will emit at a divergence angle (ϕ_{div}) described by the following expression [27,29,30]:

$$\phi_{\text{div}} \approx \frac{\upsilon_{\text{NIR1}}\theta_{\text{NIR1}} + \upsilon_{\text{NIR2}}\theta_{\text{NIR2}}}{\upsilon_{\text{XUV}}}, \tag{2}$$

where υ_{NIR1} and υ_{NIR2} are the frequencies of the NIR photons involved in the wave-mixing pathway, θ_{NIR1} and θ_{NIR2} are the crossing angles at which the NIR beams intersect the XUV in the target cell, and υ_{XUV} is the frequency of the initial XUV excitation. Multiple wave-mixing pathways composed of photons of different frequencies can emit at the same energy, augmenting the angular divergence of the wave-mixing signals [28]. However, the intensity of emission is enhanced when each photon involved in the wave-mixing process is resonant with a transition in the medium [58,59], resulting in a preference for pathways mediated by one-photon, dipole forbidden (dark) states. Two NIR photons couple one photon, dipole allowed (bright) states via dark states, leading to the emission of XUV photons at the energies of the Rydberg states observed in the photoabsorption spectrum. Calculations described in Sec. II B suggest that the viable intermediary dark states are located below the emitting state in energy, as depicted in Fig. 3(a).

A representative photon energy-calibrated CCD camera image taken at the temporal overlap of all three pulses is shown in Fig. 3(b). The negative absorbance features (blue)

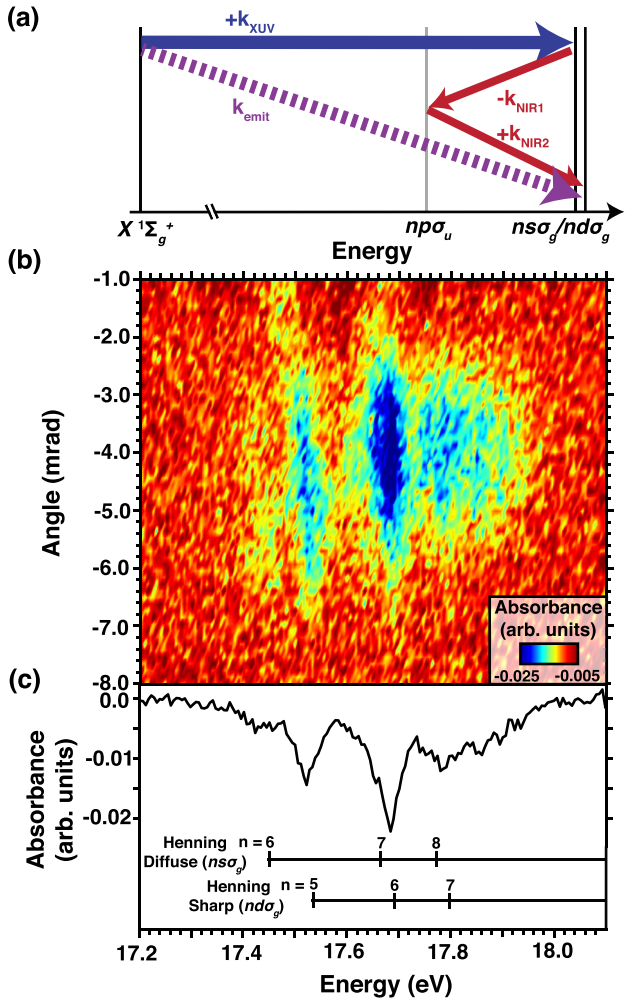

FIG. 3. Background-free wave-mixing signals are detected by an x-ray CCD camera at spatial and temporal overlap of all three pulses. (a) A wave-vector phase-matching diagram demonstrating the generation of spatially isolated four-wave-mixing signals (dashed purple arrow) from an XUV pulse train (thick blue arrow) and two NIR pulses (thin red arrows). Not to scale. (b) An x-ray charge coupled device (CCD) image plotted as a function of photon energy and phase-matching divergence angle reveals multiple wave-mixing emission features (blue). (c). An angle-integrated trace taken from this camera image can be compared to literature photoabsorption spectra for spectral assignment. The observed emission features correspond primarily to Rydberg series that converge to the ionic $\tilde{B}\ ^2\Sigma_u^+$ limit, with the Henning sharp series representing the dominant contribution.

observed in the camera image indicate the generation of new XUV light due to wave-mixing emission. The spatial dimension of the camera image is plotted as a function of the angle of divergence relative to the harmonics, which have been translated off of the CCD chip to minimize interference from on-axis (0 mrad) signals. Note that wave-mixing pathways that incorporate two time-coincident NIR pulses can emit at both negative and positive divergence angles, depending on the arbitrarily assigned NIR pulse order. Although discrete emission lines can be discerned as a function of photon energy, the wave-mixing features are broad in divergence angle. The angular divergence of these wave-mixing features

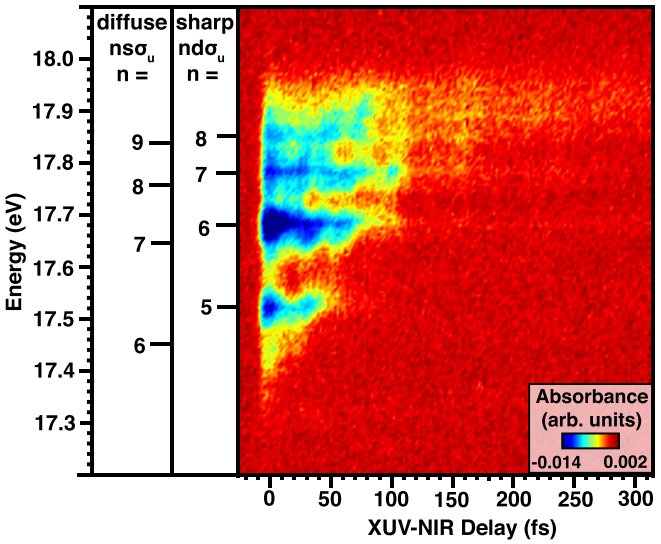

FIG. 4. Wave-mixing signals are plotted as a function of photon energy and XUV-NIR delay, revealing both oscillatory features and emission state-dependent decays. State assignments are provided to the left of the figure. The decay times associated with the wave-mixing signals emitting from the Henning sharp series lengthen with increasing principal quantum number.

[Fig. 3(b)] primarily reflects the angular spread of the incident XUV beam, but the divergence also may be broadened to a lesser extent by additional FWM pathways that emit at similar energies.

In Fig. 3(c), a spectral trace of the wave-mixing emission shown in Fig. 3(b) is obtained by integrating over the negative absorbance features in the angular range of 2.7–5.8 mrad. The most prominent features arise at energies associated with members of the Henning sharp series with principal quantum numbers from $n = 5$ to $n = 8$. Weaker features mirroring these strong wave-mixing signals at slightly lower photon energies appear to emit at the energies of the Henning diffuse series. While emission from the lowest member of the Henning diffuse series ($n = 6$) can be distinguished from the nearby Henning sharp series feature ($n = 5$), the spectral resolution of the apparatus is insufficient to resolve the majority of adjacent Henning diffuse and sharp emission features, particularly as the states become more finely spaced in the approach to the ionization threshold (IP). Consequently, the wave-mixing emission features reported here exhibit broader spectral linewidths than would be expected for members of the Henning sharp series alone given previous synchrotron measurements [40].

B. Ultrafast dynamics of autoionizing Rydberg states

The XUV-induced coherent superposition decays with the dephasing time, or polarization lifetime, of the constituent Rydberg states [27]. The temporal evolution of the XUV-induced Rydberg state coherence can be monitored by plotting angle-integrated wave-mixing signals as a function of the delay between the XUV and time-coincident NIR pulses. Figure 4 provides a false color plot depicting the emission features in Fig. 3(c) as a function of both photon energy and

XUV-NIR delay. As in the CCD camera image [Fig. 3(b)], wave-mixing signals appear as negative absorbance features at energies associated with Rydberg state resonances. These emission signals exhibit both appreciable decays and oscillations indicative of the XUV-induced coherence within the few hundred femtosecond time period investigated in this experiment. As in previous transient wave-mixing experiments that probed manifolds of autoionizing states [27], the duration of the wave-mixing signals increases with the photon energy of the emission state, reminiscent of the well-known $(n^*)^3$ trend for autoionizing state lifetimes [27,60].

To assess the timescales of the wave-mixing decays, the emission signals are integrated over a narrow energy window corresponding to the Henning sharp states and fit to a convolution of the instrumental response and an exponential decay using a least squares algorithm (Fig. 5). The application of this fitting procedure to three different datasets (Appendix B) yields decays of 33 ± 6, 53 ± 2, and 94 ± 2 fs for the features emitting from the $n = 5$, $n = 6$, and $n = 7$ members of the Henning sharp series, respectively. Integrating over smaller angular regions of Fig. 3(b) does not appreciably change the extracted decays. As expected, these time constants reflect the proportional increase in autoionizing state lifetime with $(n^*)^3$ [60]. However, these measured decays are not consistent with the calculated lifetimes of the Henning sharp series, which will be shown in Sec. III C to decay on timescales more than an order of magnitude longer than observed here. The decay of the wave-mixing emission instead corresponds to lifetimes of the Henning diffuse series, as discussed further in the following sections.

Oscillations have been observed in similar XUV wave-mixing experiments investigating both atomic [27,31,32] and molecular systems [21,30]. Here, wave-mixing oscillations are most pronounced in the short-lived features emitting from lower-lying members of the Henning sharp series. A Fourier transform taken along the delay axis of the transient wave-mixing spectrum shown in Fig. 4 reveals frequency components at energies associated with wave-mixing emission [Fig. 6(a)]. Although broad, the dominant frequency components in the Fourier spectra roughly correspond to energy differences between members of the Rydberg series that comprise the initial XUV-induced coherent superposition of states. The evolution of this coherence is probed by the time-coincident NIR pulses, which couple members of the coherence back to the Rydberg manifold via a resonant dark state, resulting in wave-mixing emission. The contribution of each member of the initial coherence to the emitted signal can be represented by a wave-mixing pathway. Multiple wave-mixing pathways can emit at the same energy, resulting in oscillations in the emission signal. As depicted in Fig. 6(b), the ~0.12 eV frequency feature obtained from the $n = 6$ Henning sharp emission signal appears to correspond to the energy difference between the $n = 7$ and $n = 8$ Henning diffuse states, both of which are members of the original XUV-induced coherence.

Note that wave-mixing pathways utilizing a Henning diffuse ($ns\sigma_u$) state cannot be distinguished from pathways involving the adjacent Henning sharp ($n'd\sigma_u$) state for the same interaction due to the breadth of the Fourier features. Moreover, frequencies associated with coherences of adjacent $ns\sigma_u$ and $n'd\sigma_u$ states are expected to appear below 0.09 eV and thus cannot be positively identified. Unlike some previous measurements [27], unity slope lines are not apparent in the transformed spectrum, indicating that wave-mixing pathways composed of degenerate photons that couple the emitting state to itself do not dominate emission in this system.

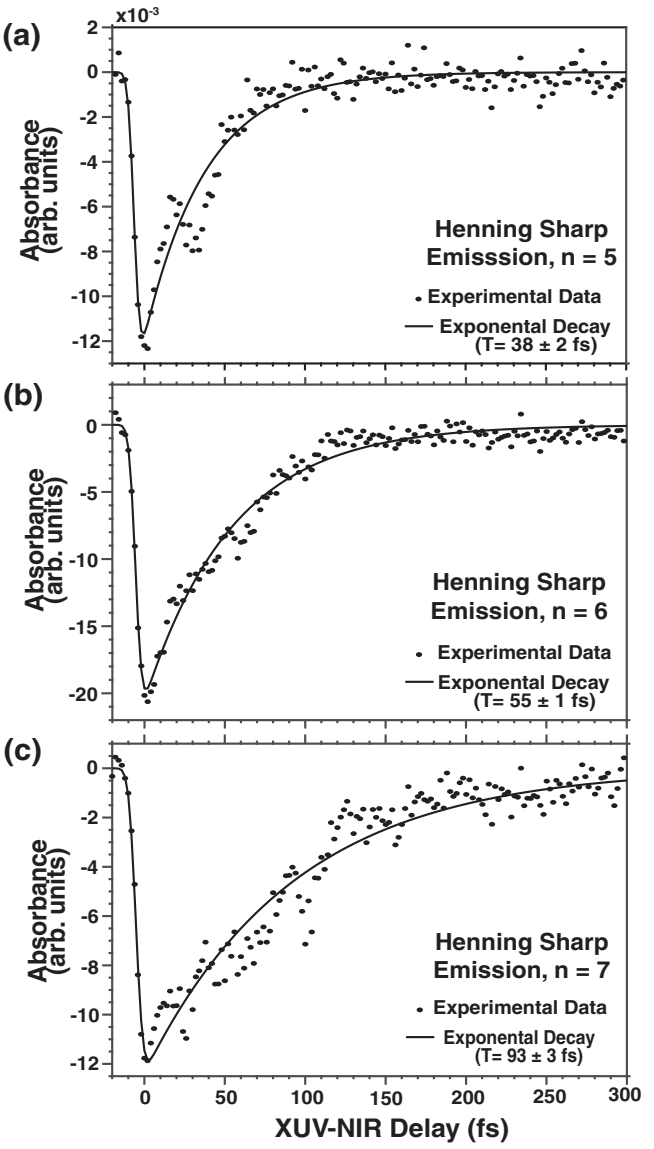

FIG. 5. Wave-mixing signals exhibit emission state-dependent ultrafast decays. Line-outs taken at the energy positions of the Henning sharp (a) $n = 5$ (17.50–17.53 eV), (b) $n = 6$ (17.67–17.70 eV), and (c) $n = 7$ (17.77–17.80 eV) states from a representative data set are fit with exponential decays, revealing decay constants that increase with principal quantum number. The dots in each of the panels represent measured experimental data while the solid lines are numerical fits. The time constants and error provided here correspond to the least squares fit of a single data set. The decay constants measured correspond with the lifetimes of the Henning diffuse states, not the sharp states from which they emit.

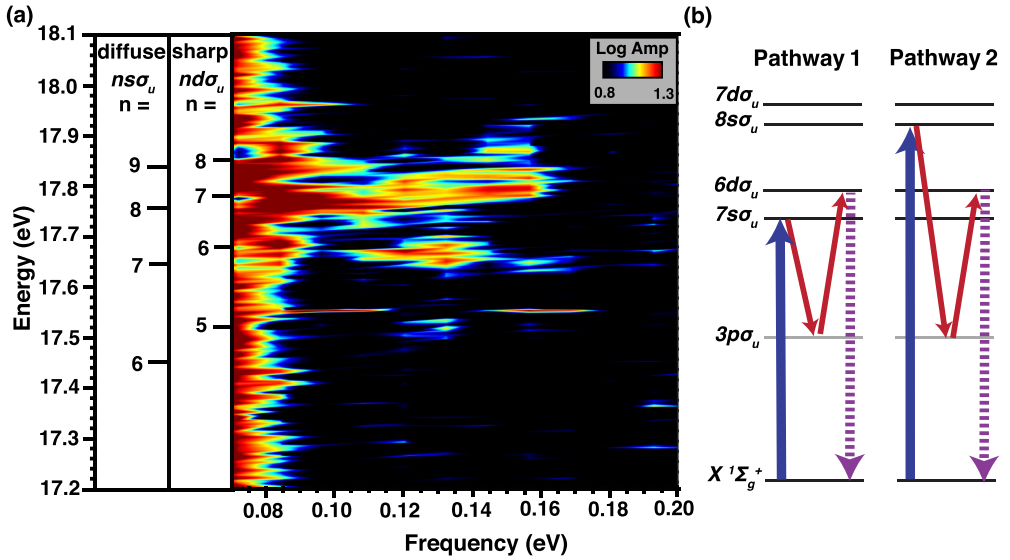

FIG. 6. (a) Fourier analysis of the delay-dependent wave-mixing emission spectrum. State assignments are provided to the left of the spectrum. Broad frequency-domain features are observed at energies associated with the Henning sharp series. (b) Interference between wave-mixing pathways built on different Rydberg series members within the XUV bandwidth leads to oscillations with frequencies consistent with those measured in the Fourier transform in the wave-mixing emission spectrum. The NIR pulses are represented by thin red arrows, while the XUV pulse and FWM emission are represented by thick blue and dashed purple arrows, respectively.

C. Theory results

In the photon energy range interrogated directly by the FWM experiment, 17.5–17.9 eV above the ground state, the calculations of the photoionization cross sections found two series of Rydberg autoionizing resonances leading to the $\tilde{B}\ ^2\Sigma_u^+$ ionization threshold. The positions and widths extracted from the Fano profile analysis for these resonances are given in Table I. The resonances in the diffuse $^1\Sigma_u^+[ns\sigma_u\,\tilde{B}\ ^2\Sigma_u^+]$ series and the sharp $^1\Sigma_u^+[nd\sigma_u\,\tilde{B}\ ^2\Sigma_u^+]$ series come in pairs with the diffuse state having quantum number n being very close to the sharp state with quantum number n–1 as is also seen in the synchrotron one-photon photoabsorption experiment [40]. In order to extract the Fano parameters for these resonances, we fit each pair of resonances independently of the other pairs. We then assumed that the fit of the Fano profile for a given pair had a common nonresonant background term, which was quadratic in the photon energy, and we further assumed that the contributions of the photoionization cross sections of the two resonances of a given pair were additive. The position and width of the $^1\Sigma_g^+[3p\sigma_u\tilde{B}\ ^2\Sigma_u^+]$ dark state are also given in Table I. We can see that the lifetimes of these autoionizing Rydberg states are strongly affected by the orbital angular momentum, with the $d\sigma_g$ being much longer lived than the $s\sigma_g$ at approximately the same energy. The $p\sigma_u$ state has an intermediate lifetime, although the specific state given with $n = 3$ would be expected to have a shorter lifetime than the corresponding $p\sigma_u$ states with higher values of n which have energies that are closer to the $s\sigma_g$ and $d\sigma_g$ states considered here.

The oscillator strengths computed using only the extended basis set calculation between the ground, diffuse, sharp, and dark states are given in Table II. The main trend seen here is that the oscillator strengths for going from the ground state to the diffuse states are consistently larger than for the transitions from the ground states to the sharp states at a similar energy. The transitions from the dark state to the sharp and diffuse states have the opposite trend, with the transitions to the sharp

TABLE I. Calculations of linewidths and corresponding lifetimes of the Henning diffuse and Henning sharp series for the $n = 6$–8 and $n = 5$–7 states, respectively, compared with experimentally measured lifetimes. Also, the computed data for the dark state are given.

	n	Width (eV)	E (eV)	Calculated lifetime (fs)	Experimental lifetime (fs)
Diffuse	6	0.02064	17.4738	31.9	33 ± 6
$^1\Sigma_u^+[ns\sigma_u\tilde{B}\ ^2\Sigma_u^+]$	7	0.01128	17.6654	58.4	53 ± 2
	8	0.00760	17.7779	86.7	94 ± 2
Sharp	5	0.00177	17.5598	372.6	
$^1\Sigma_u^+[nd\sigma_u\tilde{B}\ ^2\Sigma_u^+]$	6	0.00045	17.7110	1457.5	
	7	0.00019	17.8059	3378.5	
Dark					
$^1\Sigma_g^+[np\sigma_u\tilde{B}\ ^2\Sigma_u^+]$	3	0.01210	15.7836	54.4	

TABLE II. Calculations of the oscillator strength between ground states, Henning diffuse and sharp series, and the $^1\Sigma_g^+[3p\sigma_u\tilde{B}\ ^2\Sigma_u^+]$ dark state located at 15.8 eV.

	n	e (eV)	XUV oscillator strength	NIR resonant energy (eV)	NIR oscillator strength to dark state
Diffuse	6	17.4738	0.020407	1.6738	0.000428
$^1\Sigma_u^+[ns\sigma_u\tilde{B}\ ^2\Sigma_u^+]$	7	17.6654	0.014138	1.8654	0.000007
	8	17.7779	0.009125	1.9779	0.00002
Sharp	5	17.5598	0.008243	1.7598	0.002355
$^1\Sigma_u^+[nd\sigma_u\tilde{B}\ ^2\Sigma_u^+]$	6	17.7110	0.001856	1.911	0.0001947
	7	17.8059	0.000745	2.0059	0.000044

states being stronger than the corresponding transitions to the diffuse states.

IV. DISCUSSION

Attosecond XUV FWM experiments on autoionizing Rydberg states of the polyatomic molecule CO_2 successfully generate wave-mixing emission signals that decay on ultrafast timescales. Although quantum beat oscillations indicative of the interference of multiple wave-mixing pathways are present in the emission features, traces taken on resonance of members of the Henning sharp series can be readily fit with single exponential decays, leading to measured decays on timescales of tens of femtoseconds. As described for similar background-free FWM measurements on autoionizing states of krypton [27] and oxygen [28], the observed decays are equivalent to the excited-state lifetimes in the absence of dephasing from interactions with other degrees of freedom. Table I compares these experimentally measured lifetimes with calculated lifetimes of members of the Henning diffuse and Henning sharp series. The calculated lifetimes for the $n = 6$–8 states of the Henning diffuse series range from 30 to 90 fs while those for the $n = 5$–7 states of the Henning sharp series decay on timescales over an order of magnitude longer in duration. Given the results of the lifetime calculations (Table I), the experimentally measured wave-mixing decays of 33 $\pm$ 6, 53 $\pm$ 2, and 94 $\pm$ 2 fs are consistent with the lifetimes of the Henning diffuse states, despite emission occurring at the energies of the Henning sharp series.

To rationalize the fact that lifetimes of the diffuse states appear in the emission of the sharp states, the FWM pathways participating in this experiment can be considered with diagrammatic perturbation theory, a method used to depict the evolution of a quantum system in response to multiple pulse interactions [1,2]. A nonlinear process, FWM emission arises from the third-order polarization of the medium and is therefore described by three perturbative light-matter interactions. As shown in Fig. 7, a resonant FWM pathway can be initiated by an XUV photon that excites CO_2 from its ground state to either a Henning diffuse or Henning sharp state. Two NIR photons then couple the XUV-excited Rydberg state to itself or other states within the NIR bandwidth via a resonant dark state, generating a third-order polarization response that results in the emission of a photon with the energy of the final state. As a result, four different types of pathways depending on the initial excitation and final emission states can be enumerated: diffuse-to-sharp pathways [Fig. 7(a)], diffuse-to-diffuse pathways [Fig. 7(b)], sharp-to-sharp pathways [Fig. 7(c)], and sharp-to-diffuse pathways [Fig. 7(d)]. For transient measurements in which the two NIR pulses are delayed with respect to the XUV pulse, the dynamics measured will encode the lifetime of the state initially excited by the XUV photon, rather than the state from which the photon emits [27].

Within the framework of perturbation theory, which may not be strictly applicable in attosecond wave-mixing experiments, the intensity of resonant FWM emission signals can be approximated by the oscillator strengths of each stepwise transition between states in the wave-mixing process, as well as the intensity of the XUV and NIR light utilized in each interaction. The FWM emission signal intensity has been shown to vary linearly with NIR intensity in previous work where only a single order of wave-mixing features was observed [25,29], validating the application of perturbation theory to these systems. Assuming that the intensity of the broadband light sources is relatively constant within the energy region of interest, the oscillator strengths of different transitions can be utilized to develop an expectation for the dominant FWM pathway. As shown in Table II, the oscillator strengths calculated for the initial XUV excitation are about 2.5–10 times larger for the Henning diffuse states than for the sharp states, indicating that the XUV-induced coherent superposition being probed is dominated primarily by the short-lived diffuse states. In contrast, oscillator strengths calculated for NIR transitions between the bright states and the $^1\Sigma_g^+[3p\sigma_u\tilde{B}\ ^2\Sigma_u^+]$ dark state located at $\sim$15.8 eV are about 5–20 times stronger for the Henning sharp series, favoring pathways that ultimately emit from these sharp states. As a result, the diffuse-to-sharp pathway depicted in Fig. 7(a) should represent the largest contribution to FWM emission, resulting in decays characteristic of the initial Henning diffuse state and emission from the final Henning sharp state. Although nonresonant interactions, higher-order processes, and strong field effects may also influence the intensity and temporal evolution of the emitted signals, we do not observe clear evidence of higher-order processes in contrast to other FWM studies [27,33]. Moreover, the pathways predicted to dominate by this perturbative approach are consistent with the experimental observations of lifetimes with timescales less than 100 fs emitting at the energies of the Henning sharp series.

As discussed above, measurement of the ultrafast lifetimes of the Henning diffuse states is a direct consequence of the resonance-enhanced nonlinear technique used to probe these

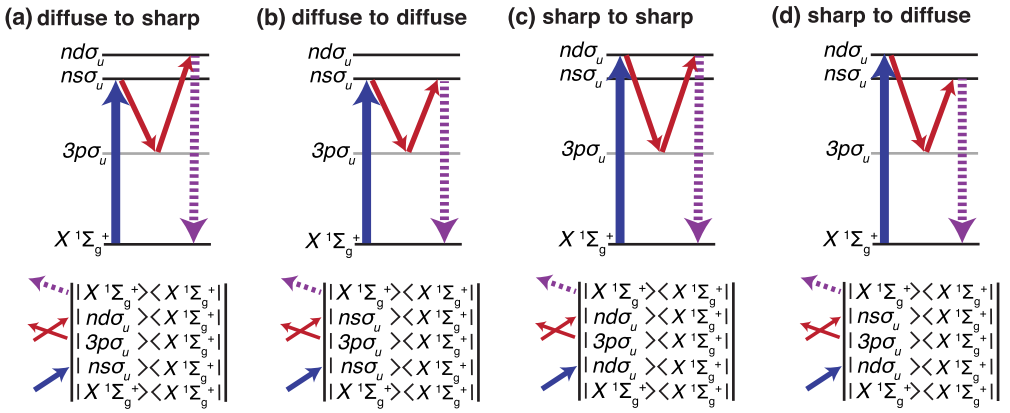

FIG. 7. Energy level and double-sided Feynman diagrams corresponding to FWM pathways composed of an XUV photon (thick blue arrows), two NIR photons (thin red arrows), and wave-mixing emission (dashed purple arrows) that couple (a) Henning diffuse to sharp states, (b) Henning diffuse to diffuse states, (c) Henning sharp to sharp states, and (d) Henning sharp to diffuse states. In all the depicted pathways, the two NIR pulses are time coincident and are delayed relative to the initial XUV pulse.

Rydberg state dynamics of CO_2. The transitions that comprise each interaction of the FWM scheme work in concert to regulate the emission intensity of individual pathways, selectively enhancing some emission signals relative to others. Favorable pathways are selected not only by the photoabsorption cross section of the state accessed by the XUV pulse, but also by additional NIR transitions between bright and dark states. Thus, attosecond XUV FWM spectroscopy permits the investigation of states that give rise to less prominent features or are obscured by spectral congestion in the linear absorption spectrum. For example, despite less-than-ideal spectral resolution, the oscillator strengths of the FWM interactions in CO_2 operate such that the short-lived, and therefore spectrally broad, Henning diffuse states emit primarily from spectrally narrow Henning sharp states without significant contamination from a long-lived emission component. Although incidental in this system, the results illustrate that, with careful consideration of intermediary dark states and transition oscillator strengths, attosecond XUV FWM spectroscopy coupled with theory can be successfully utilized to emphasize the dynamic signatures from otherwise poorly accessible states.

V. CONCLUSIONS

In this work, experiment and theory have combined to elucidate the complex nonlinear spectroscopy of short-lived, autoionizing Rydberg states located between 17.3 and 18.1 eV in the polyatomic greenhouse gas, CO_2. Experimentally, attosecond XUV FWM spectroscopy, a recently developed nonlinear technique that utilizes a noncollinear beam geometry between a short train of subfemtosecond XUV pulses and two few-cycle NIR pulses, generates background-free FWM signals in a complex spectral region dominated by the $ns\sigma_g$ character Henning diffuse and the $nd\sigma_g$ character Henning sharp Rydberg series. Transient FWM signals predominantly emit from the $n = 5$–7 members of the spectrally narrow Henning sharp series from 17.3 to 18.1 eV.

Theoretical calculations indicate that the experimentally measured decays of 33 ± 6, 53 ± 2, and 94 ± 2 fs correspond to the lifetimes of the $n = 6$–8 states of the Henning diffuse series, respectively. Following identification of the $^1\Sigma_g^+[3p\sigma_u\tilde{B}\ ^2\Sigma_u^+]$ dark state as the best candidate to mediate the wave-mixing process, the oscillator strengths of transitions between all states potentially involved in resonant FWM pathways were calculated to rationalize the dominance of the Henning diffuse states in transient wave-mixing measurements. Large ground-to-diffuse state oscillator strengths combined with substantial oscillator strength transitions between the dark state and the Henning sharp states result in the selection of pathways characterized by an initial XUV excitation to the Henning diffuse states, but emission from the Henning sharp states. Consistent with the reported experimental lifetimes, these pathways generate FWM signals that encode the lifetimes of the Henning diffuse states in the FWM emissions of the sharp states.

This work broadly demonstrates that, with the correct set of coupling strengths, the properties of short-lived, spectrally broad features can be successfully measured using emission from more spectrally narrow resonances, reducing the impact of spectral congestion. Therefore, these

TABLE III. The data collection parameters employed for the three experimental datasets examined in this work.

Dataset	Delay range (fs)	Delay step size (fs)	Exposure time (s)	Number of images	Pulses per delay	Backing pressure (Torr)
1: 2/27/20	−15–255	1 fs: −15–67 fs 2 fs: 68–255 fs	1.5	10	15000	4
2: 7/29/20	−14–146	1 fs	1.2	10	12000	9
3: 7/30/20	−25–315	2 fs	1.2	15	18000	11

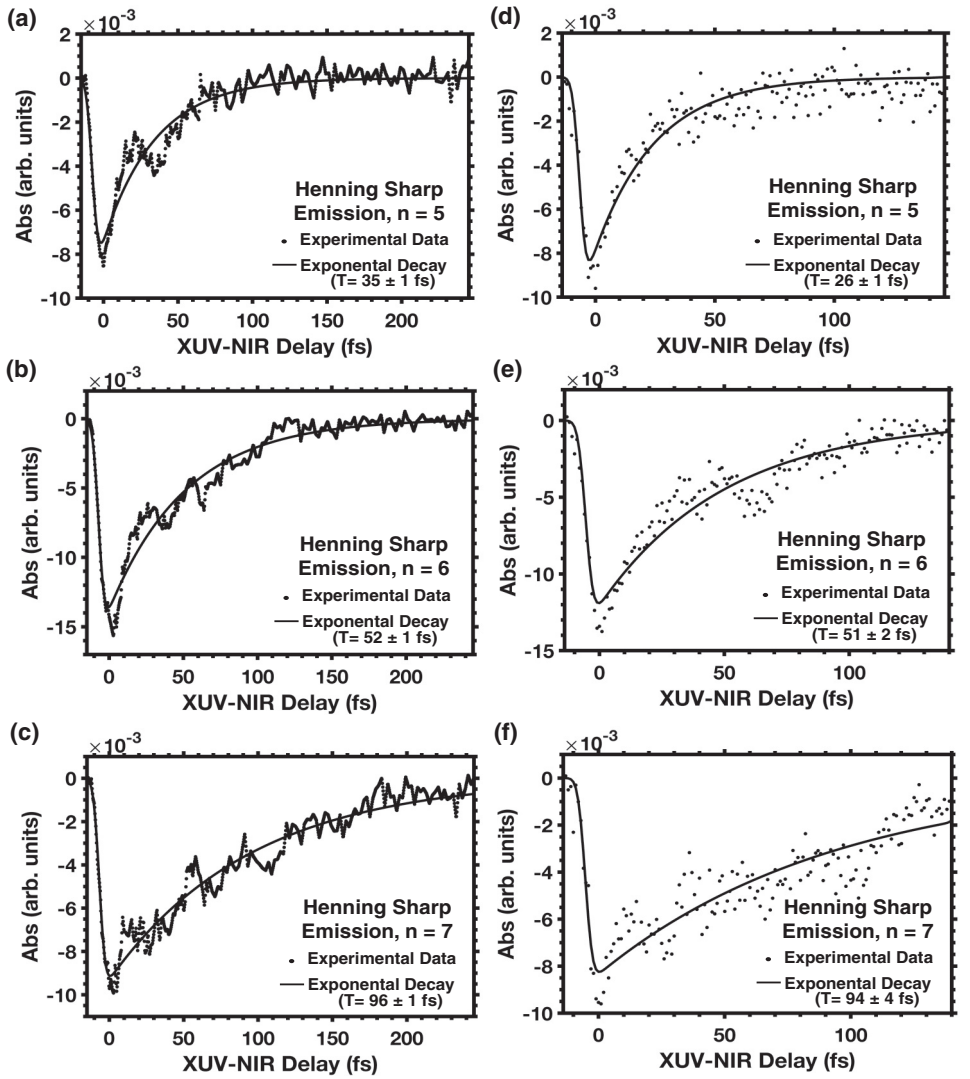

FIG. 8. Delay-dependent traces of wave-mixing emission features observed at the energy positions of the Henning sharp (a) $n = 5$ (17.49–17.55 eV), (b) $n = 6$ (17.66–17.70 eV), and (c) $n = 7$ (17.77–17.80 eV) states in dataset 1 and the (d) $n = 5$ (17.48–17.54 eV), (e) $n = 6$ (17.65–17.71 eV), and (f) $n = 7$ (17.76–17.81 eV) states in dataset 2. The dots in each of the panels represent measured experimental data while the solid lines are numerical fits. The time constants and errors provided here correspond to the least squares fit of a single data set. The data points of dataset 1 were interpolated to obtain a constant step size for analysis. The decay constants measured correspond with the lifetimes of the Henning diffuse states, not the sharp states from which they emit.

results not only provide insights into the decay dynamics of autoionizing states in a highly significant polyatomic molecule, but also illustrate a powerful application of experimental and theoretical attosecond XUV FWM analysis that can be utilized in more complex chemical systems.

ACKNOWLEDGMENTS

This work is performed under the auspices of the U.S. Department of Energy (DOE), Office of Science, Office of Basic Energy Sciences, Chemical Sciences, Geosciences, and Biosciences Division under Contract No. DEAC02-05CH11231. This research used resources of the Lawrencium computational cluster resource provided by the IT Division at the LBNL and the National Energy Research Scientific Computing Center, a DOE Office of Science User Facility supported by the Office of Science of the U.S. Department of Energy under Contract No. DE-AC02-05CH11231 using NERSC Award No. BES-ERCAP0020143. A.P.F. acknowledges support from the National Science Foundation Graduate Research Fellowship Program and Y.-C.L. acknowledges financial support from the Taiwan Ministry of Education. J.D.G. is grateful to the Arnold and Mabel Beckman Foundation for support as an Arnold O. Beckman Postdoctoral Fellow.

A.P.F., Y.-C.L., J.D.G., S.R.L., and D.M.N. designed the experiments; A.P.F., Y.-C.L., and J.D.G. performed the FWM experiments; A.P.F. and Y.-C.L. analyzed the experimental data. R.R.L. and C.W.M. determined the theoretical approach needed to explain the experimental results and R.R.L.

TABLE IV. The experimentally measured wave-mixing decays are fit to a convolution of the instrumental response and an exponential decay.

	1: 2/27/20	2: 7/29/20	3: 7/30/20	Average
$n = 5$	35 ± 1 fs	26 ± 1 fs	38 ± 2 fs	33 ± 6 fs
$n = 6$	52 ± 1 fs	51 ± 2 fs	55 ± 1 fs	53 ± 2 fs
$n = 7$	96 ± 1 fs	94 ± 4 fs	93 ± 3 fs	94 ± 2 fs

performed the calculations. A.P.F., Y.-C.L., J.D.G., R.R.L., C.W.M., S.R.L., and D.M.N. discussed results; A.P.F, Y.-C.L., and R.R.L. wrote the paper.

APPENDIX A: EXPERIMENTAL PARAMETERS

A total of three datasets were collected up to five months apart to verify experimental findings. Table III summarizes the parameters utilized for each of the three datasets. For all experiments, one averaged CCD camera image of the signal with all three laser beams present ($I_{\mathrm{NIR\ ON}}$) and one averaged image with the two NIR pulses absent ($I_{\mathrm{NIR\ OFF}}$) were recorded for each delay. Both images are constructed from the same number of laser pulses per delay, which can be calculated using the following equation:

$$\text{pulses per delay} = \text{exposure time (s)} \times \text{repetition rate (Hz)} \times \text{number of images}, \tag{A1}$$

where the repetition rate is 1000 Hz. The exposure time refers to the length of time the CCD camera collects photons to generate a single image, which is then averaged with other images taken at the same delay to generate the averaged image used for analysis. Values for the exposure time and the number of images can be found in Table III. Several hours of stable signal are required to complete each dataset. Note that backing pressure refers to the pressure of CO_2 gas measured in the delivery lines before entering the vacuum chamber. All figures shown in the manuscript originate from dataset 3.

APPENDIX B: FITTING RESULTS OF ADDITIONAL DATASETS

Wave-mixing emission features at the energies of the Henning sharp $n = 5$–7 states observed in datasets 1 and 2 are fit to a convolution of the instrumental response and an exponential decay using a least squares algorithm in Fig. 8. Similar fits for dataset 3 are provided in Fig. 6 of the main text. The results of performing this fitting procedure on all datasets are summarized in Table IV. The reported decays represent the mean and standard deviation of the fits of the three datasets.

[1] S. Mukamel, *Principles of Nonlinear Optical Spectroscopy* (Oxford University Press, New York, 1995).

[2] P. Hamm and M. T. Zanni, *Concepts and Methods of 2D Infrared Spectroscopy* (Cambridge University Press, Cambridge, 2011).

[3] G. S. Schlau-Cohen, T. R. Calhoun, N. S. Ginsberg, E. L. Read, M. Ballottari, R. Bassi, R. van Grondelle, and G. R. Fleming, J. Phys. Chem. B **113**, 15352 (2009).

[4] K. Ramasesha, L. De Marco, A. Mandal, and A. Tokmakoff, Nat. Chem. **5**, 935 (2013).

[5] M. K. Petti, J. P. Lomont, M. Maj, and M. T. Zanni, J. Phys. Chem. B **122**, 1771 (2018).

[6] G. Moody, C. K. Dass, K. Hao, C.-H. Chen, L.-J. Li, A. Singh, K. Tran, G. Clark, X. Xu, G. Berghäuser *et al.*, Nat. Commun. **6**, 8315 (2015).

[7] S. Coen, A. H. L. Chau, R. Leonhardt, J. D. Harvey, J. C. Knight, W. J. Wadsworth, and P. S. J. Russell, J. Opt. Soc. Am. B **19**, 753 (2002).

[8] L. Drescher, O. Kornilov, T. Witting, V. Shokeen, M. J. J. Vrakking, and B. Schütte, Nat. Photonics **15**, 263 (2021).

[9] T. E. Glover, D. M. Fritz, M. Cammarata, T. K. Allison, S. Coh, J. M. Feldkamp, H. Lemke, D. Zhu, Y. Feng, R. N. Coffee *et al.*, Nature (London) **488**, 603 (2012).

[10] F. Bencivenga, R. Cucini, F. Capotondi, A. Battistoni, R. Mincigrucci, E. Giangrisostomi, A. Gessini, M. Manfredda, I. P. Nikolov, E. Pedersoli *et al.*, Nature (London) **520**, 205 (2015).

[11] L. Foglia, F. Capotondi, R. Mincigrucci, D. Naumenko, E. Pedersoli, A. Simoncig, G. Kurdi, A. Calvi, M. Manfredda, L. Raimondi *et al.*, Phys. Rev. Lett. **120**, 263901 (2018).

[12] R. Mincigrucci, L. Foglia, D. Naumenko, E. Pedersoli, A. Simoncig, R. Cucini, A. Gessini, M. Kiskinova, G. Kurdi, N. Mahne *et al.*, Nucl. Instrum. Methods Phys. Res., Sect. A **907**, 132 (2018).

[13] J. L. Krause, K. J. Schafer, and K. C. Kulander, Phys. Rev. Lett. **68**, 3535 (1992).

[14] P. B. Corkum, Phys. Rev. Lett. **71**, 1994 (1993).

[15] M. Hentschel, R. Kienberger, C. Spielmann, G. A. Reider, N. Milosevic, T. Brabec, P. Corkum, U. Heinzmann, M. Drescher, and F. Krausz, Nature (London) **414**, 509 (2001).

[16] E. Goulielmakis, Z.-H. Loh, A. Wirth, R. Santra, N. Rohringer, V. S. Yakovlev, S. Zherebtsov, T. Pfeifer, A. M. Azzeer, M. F. Kling *et al.*, Nature (London) **466**, 739 (2010).

[17] W. Cao, E. R. Warrick, D. M. Neumark, and S. R. Leone, New J. Phys. **18**, 013041 (2016).

[18] Y. Kobayashi, M. Reduzzi, K. F. Chang, H. Timmers, D. M. Neumark, and S. R. Leone, Phys. Rev. Lett. **120**, 233201 (2018).

[19] G. Sansone, F. Kelkensberg, J. F. Pérez-Torres, F. Morales, M. F. Kling, W. Siu, O. Ghafur, P. Johnsson, M. Swoboda, E. Benedetti *et al.*, Nature (London) **465**, 763 (2010).

[20] F. Calegari, D. Ayuso, A. Trabattoni, L. Belshaw, S. De Camillis, S. Anumula, F. Frassetto, L. Poletto, A. Palacios, P. Decleva *et al.*, Science **346**, 336 (2014).

[21] W. Cao, E. R. Warrick, A. Fidler, S. R. Leone, and D. M. Neumark, Phys. Rev. A **97**, 023401 (2018).

[22] M. Schultze, E. M. Bothschafter, A. Sommer, S. Holzner, W. Schweinberger, M. Fiess, M. Hofstetter, R. Kienberger, V. Apalkov, V. S. Yakovlev *et al.*, Nature (London) **493**, 75 (2013).

[23] M. Schultze, K. Ramasesha, C. D. Pemmaraju, S. A. Sato, D. Whitmore, A. Gandman, J. S. Prell, L. J. Borja, D. Prendergast, K. Yabana *et al.*, Science. **346**, 1348 (2014).

[24] M. Zürch, H.-T. Chang, L. J. Borja, P. M. Kraus, S. K. Cushing, A. Gandman, C. J. Kaplan, M. H. Oh, J. S. Prell, D. Prendergast *et al.*, Nat. Commun. **8**, 15734 (2017).
[25] W. Cao, E. R. Warrick, A. Fidler, S. R. Leone, and D. M. Neumark, Phys. Rev. A **94**, 021802(R) (2016).
[26] W. Cao, E. R. Warrick, A. Fidler, D. M. Neumark, and S. R. Leone, Phys. Rev. A **94**, 053846 (2016).
[27] A. P. Fidler, H. J. B. Marroux, E. R. Warrick, E. Bloch, W. Cao, S. R. Leone, and D. M. Neumark, J. Chem. Phys. **151**, 114305 (2019).
[28] Y. C. Lin, A. P. Fidler, A. Sandhu, R. R. Lucchese, C. W. McCurdy, S. R. Leone, and D. M. Neumark, Faraday Discuss. **228**, 537 (2021).
[29] J. D. Gaynor, A. P. Fidler, Y.-C. Lin, H.-T. Chang, M. Zuerch, D. M. Neumark, and S. R. Leone, Phys. Rev. B **103**, 245140 (2021).
[30] E. R. Warrick, A. Fidler, W. Cao, E. Bloch, D. M. Neumark, and S. R. Leone, Faraday Discuss. **212**, 157 (2018).
[31] A. P. Fidler, E. R. Warrick, H. J. B. Marroux, E. Bloch, D. M. Neumark, and S. R. Leone, J. Phys. Photonics **2**, 034003 (2020).
[32] H. J. B. Marroux, A. P. Fidler, D. M. Neumark, and S. R. Leone, Sci. Adv. **4**, eaau3783 (2018).
[33] A. P. Fidler, S. J. Camp, E. R. Warrick, E. Bloch, H. J. B. Marroux, D. M. Neumark, K. J. Schafer, M. B. Gaarde, and S. R. Leone, Nat. Commun. **10**, 1384 (2019).
[34] D. A. Lashof and D. R. Ahujah, Nature (London) **344**, 529 (1990).
[35] Y. Tanaka and M. Ogawa, Can. J. Phys. **40**, 879 (1962).
[36] G. R. Cook, P. H. Metzger, and M. Ogawa, J. Chem. Phys. **44**, 2935 (1966).
[37] V. H. Dibeler and J. A. Walker, J. Opt. Soc. Am. **57**, 1007 (1967).
[38] L. S. Wang, J. E. Reutt, Y. T. Lee, and D. A. Shirley, J. Electron Spectrosc. Relat. Phenom. **47**, 167 (1988).
[39] A. C. Parr, P. M. Dehmer, and J. L. Dehmer, J. Chem. Phys **100**, 8768 (1994).
[40] D. A. Shaw, D. M. P. Holland, M. A. Hayes, M. A. MacDonald, A. Hopkirk, and S. M. McSweeney, Chem. Phys. **198**, 381 (1995).
[41] J. Liu, M. Hochlaf, and C. Y. Ng, J. Chem. Phys. **113**, 7988 (2000).
[42] F. J. Furch, S. Birkner, J. H. Jungmann, F. Kelkensberg, C. P. Schulz, A. Rouzée, and M. J. J. Vrakking, J. Chem. Phys. **139**, 124309 (2013).
[43] H. Timmers, Z. Li, N. Shivaram, R. Santra, O. Vendrell, and A. Sandhu, Phys. Rev. Lett. **113**, 113003 (2014).
[44] D. Biswas, J. K. Wood, A. C. Plunkett, and A. S. Sandhu, Bull. Am. Phys. Soc. **67**, V01.00147 (2022).
[45] H. Timmers, Y. Kobayashi, K. F. Chang, M. Reduzzi, D. M. Neumark, and S. R. Leone, Opt. Lett. **42**, 811 (2017).
[46] Z. Chang, P. B. Corkum, and S. R. Leone, J. Opt. Soc. Am. B **33**, 1081 (2016).
[47] R. E. Stratmann and R. R. Lucchese, J. Chem. Phys. **102**, 8493 (1995).
[48] R. E. Stratmann, R. W. Zurales, and R. R. Lucchese, J. Chem. Phys **104**, 8989 (1996).
[49] C. Jin, A.-T. Le, S.-F. Zhao, R. R. Lucchese, and C. D. Lin, Phys. Rev. A **81**, 033421 (2010).
[50] R. R. Lucchese, H. Fukuzawa, X. J. Liu, T. Teranishi, N. Saito, and K. Ueda, J. Phys. B: At., Mol. Opt. Phys. **45**, 194014 (2012).
[51] G. Herzberg, *Molecular Spectra and Molecular Structure. III. Electronic Spectra and Electronic Structure of Polyatomic Molecules* (Van Nostrand–Reinhold, New York, 1966).
[52] T. H. Dunning, J. Chem. Phys. **90**, 1007 (1989).
[53] R. A. Kendall, T. H. Dunning, and R. J. Harrison, J. Chem. Phys. **96**, 6796 (1992).
[54] H. J. Werner, P. J. Knowles, G. Knizia, F. R. Manby, and M. Schütz, Wiley Interdiscip. Rev.: Comput. Mol. Sci. **2**, 242 (2012).
[55] H. J. Werner, P. J. Knowles, G. Knizia, F. R. Manby, M. Schütz, P. Celani, W. Györffy, D. Kats, T. Korona, R. Lindh *et al.*, MOLPRO, VERSION 2015.1, a package of *ab initio* programs.
[56] U. Fano, Phys. Rev. **124**, 1866 (1961).
[57] K. Kaufmann, W. Baumeister, and M. Jungen, J. Phys. B: At., Mol. Opt. Phys. **22**, 2223 (1989).
[58] J. L. Oudar and Y. R. Shen, Phys. Rev. A **22**, 1141 (1980).
[59] J. C. Wright, Annu. Rev. Phys. Chem. **62**, 209 (2011).
[60] W. Demtroder, *Atoms, Molecules, and Photons* (Springer, Berlin, 2006).